

Cosmic Calipers: Precise and Accurate Neutron Star Radius Measurements with Next-Generation Gravitational Wave Detectors

Sanika Khadkikar,¹ Ish Gupta,¹ Rahul Kashyap,^{1,2} Koustav Chandra,¹ Rossella Gamba,^{1,3} and Bangalore S. Sathyaprakash¹

¹*Institute for Gravitation and the Cosmos, Department of Physics, Pennsylvania State University, University Park, PA 16802, USA*

²*Department of Physics, Indian Institute of Technology Bombay, Mumbai 400076, India*

³*Department of Physics, University of California, Berkeley, CA 94720, USA*

Gravitational waves from merging binary neutron stars carry characteristic information about their astrophysical properties, including masses and tidal deformabilities, that are needed to infer their radii. In this study, we use Bayesian inference to quantify the precision with which radius can be inferred with upgrades in the current gravitational wave detectors and next-generation observatories such as the Einstein Telescope and Cosmic Explorer. We assign evidences for a set of plausible equations of state, which are then used as weights to obtain radius posteriors. We find that prior choices and the loudness of observed signals limit the precision and accuracy of inferred radii by current detectors. In contrast, next-generation observatories can resolve the radius precisely and accurately, across most of the mass range to within $\lesssim 5\%$ for both soft and stiff equations of state. We also explore how the choice of the neutron star mass prior can influence the inferred masses and potentially affect radii measurements, finding that choosing an astrophysically motivated prior does not notably impact an individual neutron star's radius measurements.

I. INTRODUCTION

Neutron stars (NSs) offer a unique environment to investigate matter at densities that exceed those of atomic nuclei, providing crucial insights into how matter behaves under such extreme conditions [1–7]. The NSs' equation of state (EoS) connects the microscopic properties of dense matter to macroscopic observables such as radii, masses, and tidal deformabilities. Astronomical observations by instruments like NICER [8] provide direct constraints on masses and radii, enabling the inverse problem of mapping these quantities to the EoS from the mass-radius (m - R) plane [9–15]. Similarly, terrestrial experiments, such as PREX, probe the neutron skin thickness of nuclei, which correlates with the NS radius [16–18].

In the same way, gravitational waves (GWs) from binary neutron star (BNS) mergers have added a complementary approach to constrain the NS radius. The observation of BNS merger events GW170817 [19] and GW190425 [20] by the Advanced LIGO and Advanced Virgo observatories [21, 22] pioneered the inference of NS radii using GW signals. Observing electromagnetic counterparts, such as gamma-ray bursts and kilonovae, can further inform source parameter estimates when combined with GW data. For example, the gamma-ray burst GRB170817A and the kilonova AT2017gfo associated with GW170817 imposed tighter constraints on the EoS and consequently, R [23–27]. For instance, recently Breschi *et al.* [28] and Koehn *et al.* [29] showed that combining GW and multi-messenger observations reduces uncertainty in R to less than 10% at the 90% credible interval [10, 11, 13, 26, 30–32].

However, constraints from GW observations remain broad due to GW170817's relatively low signal-to-noise ratio (SNR), a limitation primarily driven by the sensi-

tivity of the detector network at the time. Planned upgrades to current GW detectors and upcoming new observatories aim to overcome these limitations. During the fifth observational run (O5), the LIGO-Virgo-KAGRA (LVK) [21, 22, 33] detectors might achieve A+ sensitivity [34]. The planned A# upgrade will maximize the scientific potential of existing LIGO facilities [35] to their limits. Further improvements in sensitivity and bandwidth will be possible with next-generation (XG) detectors like the Cosmic Explorers (CEs) [36–38] and the Einstein Telescope (ET) [39–41]. These will not only lead to relatively higher BNS detection rates but also more precise parameter measurements as compared to current results [42].

Several studies [43–53] have employed hierarchical inference and Bayesian model selection to constrain the EoS and infer NS radii. Some studies have specifically examined the radius measurement capabilities of XG detectors using these methods. For example, Ghosh *et al.* [54] and Pradhan *et al.* [55, 56] estimated the uncertainty on $R_{1.4}$ ¹ using 50 (10) simulated BNS events, finding uncertainties of ~ 2 – 3% when a single XG detector is used. Similarly, using methods presented in Finstad *et al.* [57], Bandopadhyay *et al.* [58] showed that it is possible to constrain the $R_{1.4}$ to less than 10 m when all the BNS events observed by the 40 km CE over a decade are considered.

Many of these studies report uncertainties for $R_{1.4}$, assuming that the radius remains nearly constant for NS masses between 1.1 and 1.6 M_{\odot} . This assumption simplifies the analysis but introduces an error of ~ 200 meters, comparable to or larger than the uncertainties expected

¹ The radius of a 1.4 M_{\odot} NS

from XG detectors [59]. While the choice of $1.4 M_{\odot}$ as a reference mass is motivated by its prevalence in the observed NS populations and similar calculations can be performed for other reference masses, quoting radius uncertainties for a given NS mass does not provide a complete description. This is because the uncertainties in R depend on the NS mass, and the commonly quoted uncertainty in $R_{1.4}$ may not apply to other masses. Therefore, evaluating the precision and accuracy of the NS radius measurement with XG detectors requires considering the mass dependence of these uncertainties.

Huxford *et al.* [60] for the first time constrained the uncertainty in the NS radius for the entire mass range allowed by the considered EoSs (APR4, APR3, and ALF2), where the lower mass limit is $1 M_{\odot}$ and the upper mass limit is determined by the respective EoS. The uncertainties were constrained to within 2%, 1%, and 0.5% for configurations with one, two, and three XG observatories using Fisher methods. Walker *et al.* [61] also obtained an uncertainty of ~ 200 m in the 1–1.97 M_{\odot} range and ~ 75 m in the 1.4–1.6 M_{\odot} mass range by applying spectral decomposition [62] to the SLy EoS and by using a Bayesian framework.

This work presents an alternative methodology for constraining NS radii using an evidence-based Bayesian model selection framework with an XG network and two planned upgrades in the current GW detectors for reference. Model selection assumes that the EoS model with the highest evidence represents the actual EoS. However, this assumption is valid only if the selected set maps the EoS space continuously and includes an infinite number of models. A discrete set of EoSs could miss regions of the parameter space where viable EoSs may exist. To avoid this, we use the dense set of models from Ref. [63] (publicly available at [64]), obtained by re-analyzing GW170817 using a spectral decomposition for the EoS. In doing so, we cover a physically motivated region of the $m - R$ space. We perform model selection over ~ 2300 EoSs and calculate their evidence. Radius samples are drawn based on these EoSs in proportion to their evidence, as described in Sec. IV A, and combined to construct a posterior on R .

Additionally, we study how NS mass priors affect radius inference for individual events. With only a few detected BNS mergers, many options exist for choosing NS mass priors. Using a prior that does not match the underlying population can bias the inferred mass values, which can further bias radius measurements. Previous studies [44, 49–51] have shown that the EoS or NS mass distribution will be biased if inferred independently of the other. This study does not aim to infer the EoS or the BNS population. Instead, we investigate whether changing the NS mass prior affects R inference for individual events. While one might expect that using a prior unlike the underlying population would strongly influence R measurements, we find that these changes do not significantly impact the resulting single event radius posteriors.

The rest of this paper is organized as follows. Sec.

II summarizes parameter inference methods used in this study. In Sec. III, we elaborate on our simulation setup by describing the GW detector networks in Sec. III A, the NS mass population used in Sec. III B, and the prior choices in Sec. III C. Sec. IV A presents our methodology for inferring NS radii using the mass and tidal parameters extracted from GW signals of BNS mergers and presents the specifics of the EoSs used for model selection in Sec. IV B. We analyze the inferred radius posterior distributions in Sec. V, summarize our conclusions, and propose future research directions in Sec. VI.

II. BRIEF REVIEW OF GRAVITATIONAL WAVE PARAMETER ESTIMATION

A. Binary Parameters and Waveform Models

The calibrated detector data, $d(t)$, for our case, can be modeled as a linear combination of detector noise, $n(t)$, and a deterministic gravitational wave (GW) signal, $h(t; \vec{\Theta})$ where the latter is parameterized by signal parameters $\vec{\Theta}$. The signal itself is expressible as a sum of the two GW polarizations $h_{+, \times}$,

$$h(t; \vec{\Theta}) = F_+ h_+ + F_{\times} h_{\times}, \quad (1)$$

where $F_{+/\times}$ are the detector’s antenna response functions, which are dependent on the source’s sky location (α, δ) and polarization angle (ψ) .

For quasi-circular binary neutron star (BNS) systems, the parameter set $\vec{\Theta}$ comprises 13 parameters: six intrinsic (component masses m_i , spin components aligned with orbital angular momentum χ_i , and tidal deformability parameters Λ_i) and seven extrinsic (luminosity distance D_L , inclination ι , polarization angle ψ , coalescence time t_c , coalescence phase ϕ_c , and sky position α, δ).

Waveform models translate these intrinsic parameters of a BNS system into GW signals using different approximations of Einstein’s field equations. Post-Newtonian (PN) models, for example, employ weak-field, low-velocity expansions and are well suited for describing the motion of neutron stars and their corresponding GW emission in the adiabatic inspiral regime [65–68]. Within this framework, relativistic corrections to the Newtonian solution are incorporated systematically order by order using the expansion parameter $x = v^2/c^2$, where v is the orbital velocity and c is the light’s speed in the vacuum. This formalism can provide a fast-to-evaluate, closed-form expression of the GW signal in the frequency domain by splitting the signal into an amplitude $\tilde{A}(f)$ and an overall phase $\Psi(f)$, assuming the following schematic form:

$$\tilde{h}(f) = \tilde{A}(f) e^{i\Psi(f)}. \quad (2)$$

To the leading order, $\tilde{A}(f)$ depends on the chirp mass, $\mathcal{M} = \eta^{3/5}(m_1 + m_2)$, the symmetric mass ratio, $\eta =$

$m_1 m_2 / (m_1 + m_2)^2$, D_L and ι whereas $\Psi(f)$ has the following schematic form:

$$\Psi(f) = 2\pi t_c - 2\phi_c - \frac{\pi}{4} + \frac{3}{128\eta x^{5/2}} \times (1 + \varphi_{\text{PP}} + \varphi_{\text{SO}} + \varphi_{\text{SS}} + \varphi_{\text{Tidal}}). \quad (3)$$

Here, φ_{PP} , φ_{SO} , φ_{SS} , and φ_{Tidal} capture contributions from point-particle, spin-orbit, spin-spin, and tidal interactions, respectively.

Tidal effects arise due to mutual deformations induced by the binary components' gravitational fields and are quantified by the tidal deformability parameter,

$$\Lambda_i \equiv \frac{\lambda_i}{m^5} = \frac{2}{3} k_2 \left(\frac{c^2 R_i}{G m_i} \right)^5, \quad (4)$$

where λ_i parametrizes how much the i^{th} NS with mass m_i and radius R_i deforms, k_2 is the second tidal Love number and G is the gravitational constant [69, 70].

The effective tidal deformability depends on the mass ratio $q = m_2/m_1 \leq 1$ and characterizes the leading order tidal phase contribution,

$$\tilde{\Lambda} = \frac{16(12q+1)\Lambda_1 + (12+q)q^4\Lambda_2}{13(1+q)^5}. \quad (5)$$

which appears as a 5PN correction compared to the leading Newtonian term and, therefore, becomes more important as the binary approaches the plunge phase, where velocities increase. Although tidal corrections appear at high post-Newtonian orders, their contribution can be measurable because NS's $\Lambda \gtrsim 100$ for realistic EoSs, contingent on the NS's mass [48, 71, 72].

Alternative waveform modelling strategies provide more accurate descriptions. For example, the effective one-body formalism combines insights from the test-particle limit with PN results to construct a unified description of the two-body problem. The EOB method reformulates the system with an effective one-body Hamiltonian, wherein a test particle moves in a deformed metric [73–75]. Since EOB models are inherently time-domain and require solving coupled differential equations, they are computationally expensive.

On the other hand, phenomenological models focus exclusively on describing the GW signal without explicitly solving equations of motion [76–78]. Constructed in the frequency domain, they are computationally efficient and, hence, widely used for data analysis. They model the inspiral waveform based on analytic PN information augmented with pseudo-PN terms, then calibrated to EOB and NR results.

Our study here employs the IMRPhenomPv2_NRTidalv2 waveform model [79, 80], an extension of IMRPhenomPv2 [81, 82]. This model incorporates tidal-phase and amplitude corrections, which are constructed using Padé resummation of PN terms (up to 2.5PN adiabatic and 3.5PN spin-quadrupole contributions [80]) and further refined through numerical relativity calibrations. These enhancements allow for improved modeling of BNS waveforms while maintaining computational efficiency.

B. Bayesian Inference

We use Bayesian inference to estimate the binary parameters $\vec{\Theta}$ from the observed gravitational wave data. According to Bayes' theorem, the posterior probability distribution of the parameters $\vec{\Theta}$ given the data d is:

$$p(\vec{\Theta} | d) = \frac{\mathcal{L}(d | \vec{\Theta})\pi(\vec{\Theta})}{\mathcal{Z}_{\text{GW}}}, \quad (6)$$

where $\mathcal{L}(d | \vec{\Theta})$ is the likelihood function, $\pi(\vec{\Theta})$ represents the prior probability distribution for the parameters, and \mathcal{Z}_{GW} is the model evidence given by:

$$\mathcal{Z}_{\text{GW}} = \int d\vec{\Theta} \mathcal{L}(d | \vec{\Theta})\pi(\vec{\Theta}). \quad (7)$$

The likelihood function quantifies how well a waveform $h(\vec{\Theta})$ describes the observed data and is typically modelled as a multivariate Gaussian. The choice of prior $\pi(\vec{\Theta})$ reflects our prior knowledge and constraints on the parameter space.

For our analysis, we use the Bayesian inference library Bilby [84–87] in conjunction with the nested sampling algorithm dynesty [88] to obtain the posterior distribution of the model parameters. Given the high computational cost of analyzing long-duration BNS signals, we use the relative binning technique [89–91] to accelerate likelihood evaluations. Relative binning improves computational efficiency as both the waveform evaluation and the sum over frequencies of the likelihood function are performed at a lower frequency resolution while maintaining the desired level of accuracy. We use the relative binning implementation in Bilby which is based on the functional form of the post-Newtonian expansion [92].

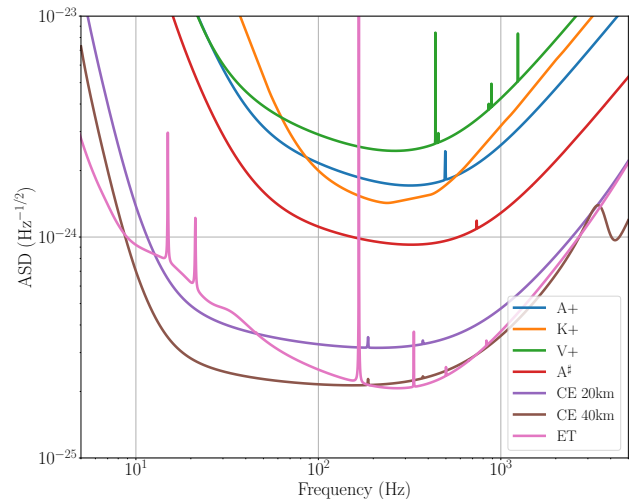


Figure 1. Amplitude spectral density (ASD) of detector noise for LIGO (A+ and A# sensitivity), Virgo (V+), KAGRA (K+), Cosmic Explorer (20 km and 40 km), and Einstein Telescope (ET) [83].

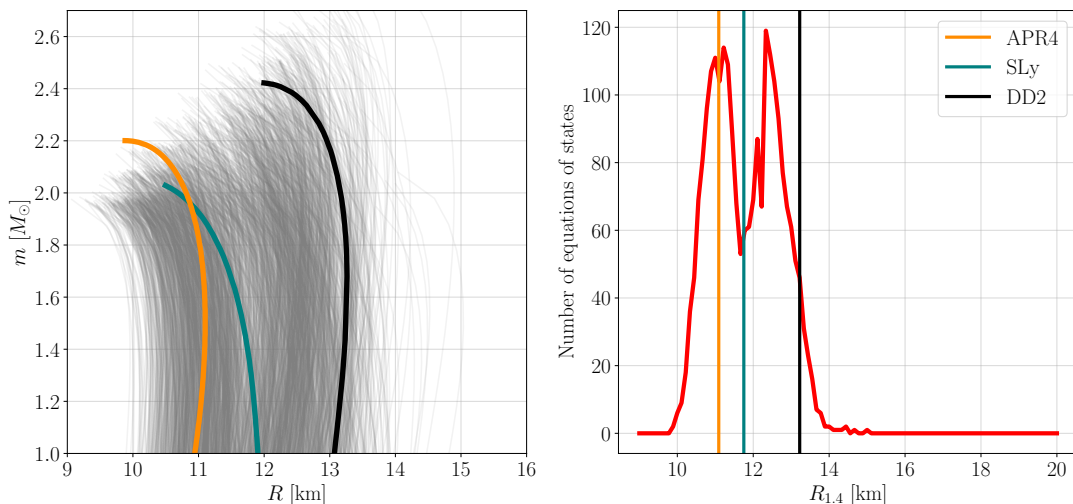


Figure 2. *Left panel:* m - R curves for the EoSs used to calculate the evidence for EoS model selection. APR4 is shown in orange, SLy in teal, and DD2 in black. The gray EoS curves are the $\mathcal{O}(2300)$ EoSs parameterized using the spectral decomposition method for the GW170817 event as a part of the public data release for [63]. *Right panel:* For the ~ 2300 EoSs considered, we calculate the number of EoSs within each radius bin for a $1.4 M_\odot$ NS, providing insight into the density distribution of EoSs in the m - R space. The APR4 EoS is represented in orange, SLy in teal, and DD2 in black. The density of EoSs is highest for radii larger than those predicted by APR4, while it is significantly lower for radii greater than those described by DD2.

Further details regarding the specific configurations used for parameter estimation, including prior choices and sampling settings, are provided in Sec. III C.

at the exact locations of the current LIGO interferometers. ET is positioned in Cascina in Italy, at the current location of the Virgo interferometer.

III. SIMULATION SETUP

A. Network Configurations

We consider three different network configurations for our study as summarized in the following (see Fig. 1 for their noise power spectrum):

- **O5:** We consider a network of LIGO Hanford, LIGO Livingston, Virgo, and KAGRA detectors operating at A+ sensitivity as the configuration for O5 [93].
- **A[#]:** The next upgrade of the LIGO detectors is the A[#] sensitivity [35]. For this configuration, in addition to LIGO Hanford and LIGO Livingston in the A[#] configuration, we have also considered LIGO India. LIGO India is a new GW interferometer currently being constructed in Aundha, India, and we assume it to be operating with A[#] sensitivity [94–96]. We do not include the Virgo or the Kagra detector for this network.
- **ECC:** To analyze the most optimistic case for detecting radius uncertainties, we use XG observatories including one triangular ET [39–41], one CE 20 km observatory, and one CE 40 km observatory [36–38]. We position the 40 km CE observatory in Hanford and the 20 km observatory in Livingston

B. Binary Population

We conduct a simulation study by using sets of 100 synthetic BNS signals. This number is consistent with the cumulative number of detections expected within a redshift of $z = 0.1$, assuming a BNS local merger rate density to be $320 \text{ Gpc}^{-3} \text{ yr}^{-1}$ [42, 97]. We sample masses for our simulated BNS signals from the galactic double Gaussian NS mass distribution model [98–102] which has means $\mu_1 = 1.35 M_\odot$ and $\mu_2 = 1.8 M_\odot$, and standard deviations $\sigma_1 = 0.08 M_\odot$ and $\sigma_2 = 0.3 M_\odot$ consistent with the BNS mass population described in [100]. The NS masses range from $1 M_\odot$ up to the maximum mass allowed by the EoSs chosen to generate the simulated signals. The spin parameters are constrained to $\chi_i \in (-0.05, 0.05)$. The simulated binaries were distributed isotropically over the binary’s orientation angle and sky location parameters.

For our simulated signals, we adopt three distinct equations of state (EoSs), strategically chosen to span the m - R space supported by the GW170817 constraints [63, 103]. A *soft* EoS, such as APR4, predicts relatively smaller tidal deformability (Λ) values for a given mass, corresponding to smaller neutron star radii. In contrast, a *stiff* EoS, exemplified by DD2, yields larger Λ values and, consequently, larger radii. The SLy EoS represents an intermediate scenario. The corresponding m - R relationships for these EoSs are depicted in the left panel

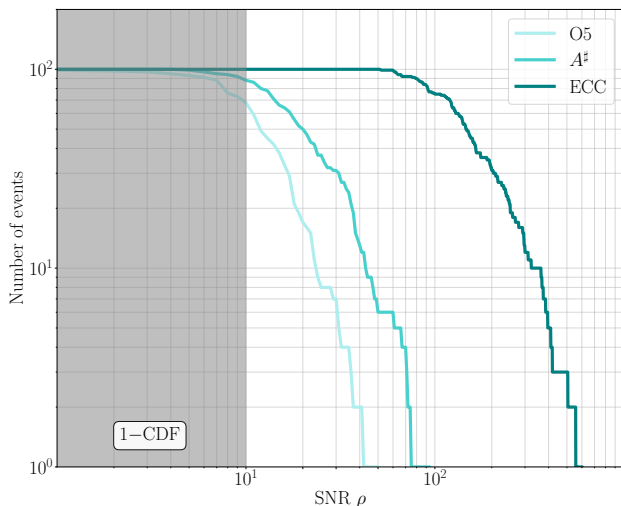


Figure 3. The scaled cumulative density function plot showing the trends in SNR ρ of the 100 simulated events based on the SNR threshold of 10 for several GW detectors chosen. The plotted numbers of detected events can be obtained using any of the three EoSs considered; however, SLy is used here for demonstration purposes and is represented in teal. Different colors represent the different networks used for this study, namely O5, A^\sharp , and ECC. While ECC detects all of the simulated events, A^\sharp detects about 90%, and O5 detects only about 70% of the simulated events.

of Fig. 2. We generate simulated gravitational wave signals based on each EoS using the waveform model `IMRPhenomPv2_NRTidalv2` and add them to data of each detector network described in Sec. III A. We do not add Gaussian noise, ensuring that our analysis is performed in zero noise, and hence, our results represent the ensemble average over many Gaussian noise realizations [104].

Fig. 3 shows the number of detectable events as a function of the SNR. ECC detects all events with SNR > 50 . In contrast, A^\sharp and O5 networks miss approximately 10% and 30% of events respectively, assuming a network SNR threshold of 10.

C. Inference Settings and Prior Choices

To obtain posterior samples, we utilize the relative binning implementation in `Bilby` with the `dynesty` sampler. Our analysis fixes the number of `walks` and `maxmcmc` at 100 and 5000, respectively. Additionally, we set the number of live points (`nlive`) to 1024 and the number of accepted steps per chain (`naccept`) to 60.

Relative binning requires a tightly constrained prior on the chirp mass \mathcal{M} , as it assumes that the most probable waveforms used in the analysis do not differ significantly. Matched-filter searches provide a reasonably good estimate of \mathcal{M} , particularly for BNS signals, due to the high density of templates in this region of parameter space [105]. Therefore, choosing a highly constrained

prior on \mathcal{M} is well justified. For the remaining parameters, we adopt the default prior choices for BNS analyses, with adjustments based on our simulated signals, as detailed in Table I [84, 106, 107]. We assume aligned spins, with maximum spin magnitudes within allowed regions of the employed waveform model. Additionally, we apply the `UniformSourceFrame` luminosity distance prior, which assumes a uniform prior in comoving volume V_c , scaled by a factor of $1/(1+z)$ to account for time dilation due to cosmic expansion, following the Planck 15 cosmology [84].

All prior choices are informed by theoretical models, physical constraints, and empirical data to reflect our prior knowledge or assumptions about the estimated parameters. When multiple viable priors exist, the Bayesian analysis pipeline can be rerun with different prior distributions. However, given the high dimensionality of the parameter space, this approach can be computationally expensive. Instead, posterior samples obtained using an initial prior $\pi_1(\vec{\theta})$ can be reweighted to reflect a different prior $\pi_2(\vec{\theta})$ using:

$$p_2(\vec{\theta}|d, H) = p_1(\vec{\theta}|d, H) \frac{\pi_2(\vec{\theta})}{\pi_1(\vec{\theta})}. \quad (8)$$

This reweighting procedure is valid when the support of $\pi_2(\vec{\theta})$ is identical to or a subset of that of $\pi_1(\vec{\theta})$. In this study, we use prior reweighting to assess the impact of different mass priors on the inferred radius constraints for individual events. Specifically, we compare two priors: (i) a double-Gaussian prior matching the exact mass distribution used to generate our simulated BNS population and (ii) an uninformative prior that is uniform over the considered mass range. Since both priors share the same support, this approach allows for directly comparing their effects.

Parameter	Shape	Limits
χ_1, χ_2	Uniform	(-0.1, 0.1)
$\cos(\theta_{JN})$	Uniform	(-1, 1)
ψ	Uniform	(0, π)
α	Uniform	(0, 2π)
δ	Cosinusoidal	($-\pi/2, \pi/2$)
D_L	Uniform in Comoving Volume	(44, 475) Mpc
$\tilde{\Lambda}$	Uniform	(0, 5000)
$\delta\tilde{\lambda}$	Uniform	(-1000, 1000)

Table I. Prior settings of signal parameters to study BNS signals.

IV. RADIUS POSTERIOR AND EOS MODEL SELECTION

We estimate posteriors for the parameter set $\vec{\Theta}$ by analyzing the simulated events using the parameter estimation methods outlined in Sec. II and Sec. III. However, Eq. (4) indicates that the neutron star radius can only

be inferred from these posteriors if the Love number k_2 is known. The value of k_2 depends on the underlying EoS governing the neutron star matter. Since the true EoS is unknown, we employ the Bayesian model selection pipeline BEOMS [108] to compute the Bayesian evidence for each candidate EoS, denoted as H_k , among the ~ 2300 EoSs considered.

For this analysis, we work in a reduced parameter space $\vec{\theta} = \tilde{\Lambda}, \mathcal{M}, \eta$, chosen specifically to facilitate the computation of EoS evidence. We begin by obtaining $\tilde{\Lambda}_k$, which is determined from the posterior samples of the chirp mass \mathcal{M} and the symmetric mass ratio η under the assumption of the k^{th} EoS. This is the model against which we compare the posterior samples of $\tilde{\Lambda}$ obtained using parameter estimation.

Given that \mathcal{M} is the most precisely estimated parameter in our inference, we simplify the analysis by fixing \mathcal{M} to its mean value, $\overline{\mathcal{M}}$. This approximation reduces the dimensionality and computational complexity of the required integrals while maintaining sufficient accuracy for our model selection procedure.

A. Evidence Calculation for EoSs

We begin by marginalizing the likelihood $\mathcal{L}(d_i|\vec{\Theta})$ over the nuisance parameters to obtain $\mathcal{L}(d_i|\vec{\theta})$ in the reduced parameter space $\vec{\theta}$. For model selection, we use it to obtain the conditional likelihood $\mathcal{L}(d_i|\vec{\theta}, H_k)$:

$$\mathcal{L}(d_i|\vec{\theta}, H_k) = \mathcal{L}(d_i|\vec{\theta})\delta(\tilde{\Lambda} - \tilde{\Lambda}_k(\overline{\mathcal{M}}, \eta)). \quad (9)$$

This ensures that only parameter space points supported by H_k contribute where H_k is the hypothesis that the k^{th} EoS describes the observed signal's tidal deformation parameters. Using Bayes' theorem, the posterior under H_k becomes

$$p(\vec{\theta}|d_i, H_k) = \frac{\mathcal{L}(d_i|\vec{\theta})\delta(\tilde{\Lambda} - \tilde{\Lambda}_k(\overline{\mathcal{M}}, \eta))\pi(\vec{\theta}|H_k)}{\mathcal{Z}(d_i|H_k)}, \quad (10)$$

where $\mathcal{Z}(d_i|H_k)$ is the model evidence,

$$\mathcal{Z}(d_i|H_k) = \int \mathcal{L}(d_i|\vec{\theta})\delta(\tilde{\Lambda} - \tilde{\Lambda}_k(\overline{\mathcal{M}}, \eta))\pi(\vec{\theta}|H_k)d\vec{\theta}. \quad (11)$$

Rewriting the evidence in terms of the posterior,

$$\mathcal{Z}(d_i|H_k) = \int \mathcal{Z}_k \delta(\tilde{\Lambda} - \tilde{\Lambda}_k(\overline{\mathcal{M}}, \eta)) p(\overline{\mathcal{M}}, \eta, \tilde{\Lambda}|d_i) d\tilde{\Lambda} d\eta, \quad (12)$$

where $p(\overline{\mathcal{M}}, \eta, \tilde{\Lambda}|d_i)$ is the joint posterior distribution, and

$$\mathcal{Z}_k = \int \mathcal{L}(d_i|\vec{\theta})\pi(\vec{\theta})d\vec{\theta} \quad (13)$$

is computed analogously to \mathcal{Z}_{GW} but in the reduced parameter space $\vec{\theta}$. We employ kernel density estimation (KDE) to obtain a smooth joint posterior $p(\overline{\mathcal{M}}, \eta, \tilde{\Lambda}|d_i)$, which, combined with the EoS, allows for evidence computation.

To infer neutron star radii, mass posteriors $p(m|d_i, H_k)$ are mapped to radius posteriors $p(R|d_i, H_k)$ for each EoS. However, a physically meaningful radius distribution should incorporate contributions from all viable EoSs, weighted by their evidences. Instead of relying solely on the most probable EoS, we compute a model-weighted posterior

$$p(R|d_i) = \sum_k p(R|d_i, H_k)p(H_k|d_i), \quad (14)$$

where

$$p(H_k|d_i) = \frac{\mathcal{Z}(d_i|H_k)P(H_k)}{\sum_j \mathcal{Z}(d_i|H_j)P(H_j)}. \quad (15)$$

Assuming all EoS are equally likely, we get:

$$p(H_k|d_i) = \frac{\mathcal{Z}(d_i|H_k)}{\sum_j \mathcal{Z}(d_i|H_j)}. \quad (16)$$

We use $\mathcal{Z}(d_i|H_k)$ and compute the final model-weighted radius posterior as:

$$p(R|d_i) = \sum_k p(R|d_i, H_k) \frac{\mathcal{Z}(d_i|H_k)}{\sum_j \mathcal{Z}(d_i|H_j)}. \quad (17)$$

To implement Eq. (17), we perform KDE over each $p(R|d_i, H_k)$ and draw samples proportional to the corresponding EoS evidence within $R \in [5, 25]$ km. With ~ 2300 EoSs considered, we generate ~ 2.3 million samples to ensure sufficient representation. For each EoS, the sample count is

$$N_k = p(H_k|d_i)N_T, \quad (18)$$

where N_T is the total sample count and $p(H_k|d_i)$ is the normalized EoS evidence. This process is repeated for all EoSs to construct the final radius posterior.

Notably, EoSs support different mass ranges; for high-mass injections, not all posterior samples are compatible with every EoS. Our algorithm filters out unsupported mass samples from the radius inference, ensuring consistency. If an EoS has too few samples for KDE, it is excluded from inference, though this is rare given the extensive EoS set (see Fig. 2). Evidences are renormalized after exclusion so that $\sum_k p(H_k|d_i) = 1$. Additionally, we examine the impact of mass prior choices on radius posteriors using the reweighting approach described in Sec. II.

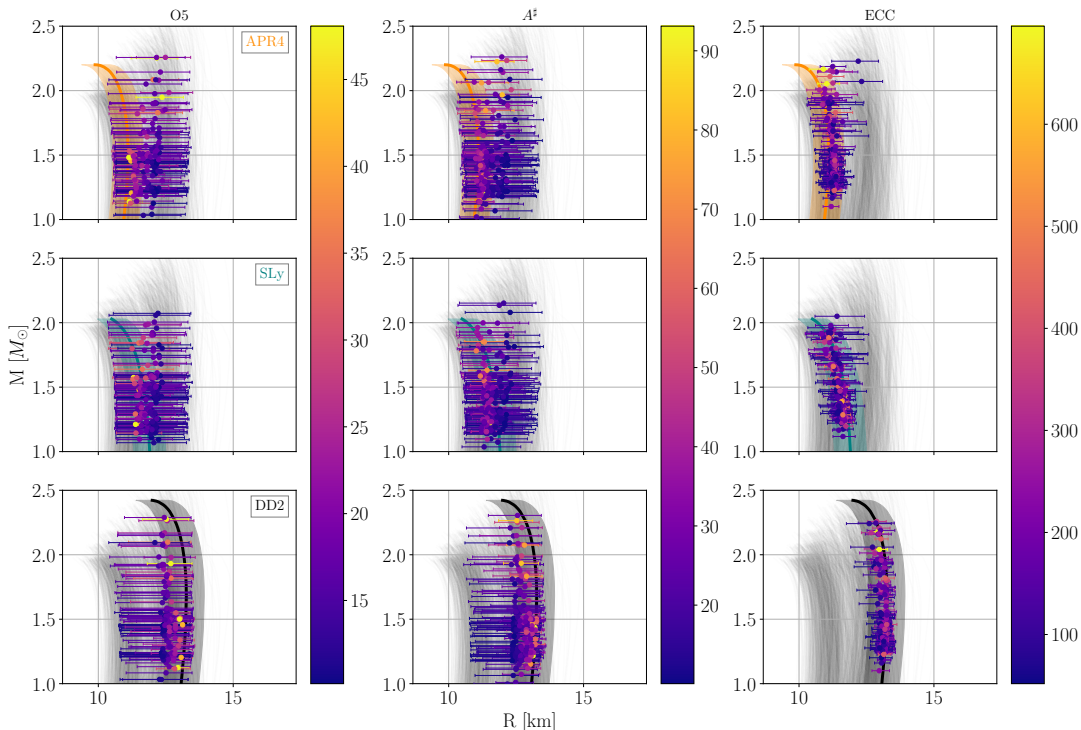


Figure 4. *Top row*: Inferred median mass vs. radius posterior for the APR EoS (orange) for individual NSs in all detected signals. Radius uncertainties (90% confidence intervals) are superposed on the EoS, with error bar colors representing SNR. Columns correspond to the O5 configuration (left), $A^\#$ (middle), and ECC (right). Gray curves depict EoSs from the spectral decomposition of GW170817. *Middle and bottom rows*: Similar plots for the SLy (teal) and DD2 (black) EoSs. Biases in radius uncertainties stem from the non-uniform EoS set (Fig. 2) and detector sensitivities. The ECC configuration constrains R most effectively, especially for the stiffer DD2 EoS, due to stronger tidal parameter effects.

B. EoSs used in simulations and model selection

We calculate model evidence for all simulated signals using ~ 2300 additional EoSs beyond those used to create the simulated signals. These additional EoSs, shown as gray curves in Fig. 2, are constructed from GW170817 constraints using the spectral decomposition method as part of Abbott *et al.* [19, 63].

Although the ensemble of EoSs effectively spans the m - R space, including the regions around the three EoSs used for simulations, its density is uneven. To illustrate this, we bin the number of EoSs according to the radius they predict for a $1.4 M_\odot$ NS into 0.1 km wide bins ranging from 9 km to 20 km, as shown in the right panel of Fig. 2. The density varies significantly, with more EoSs clustered around APR4 compared to SLy or DD2. This clustering increases the number of EoSs resembling APR4, which broadens the radius uncertainties for signals simulated using APR4. In contrast, the sparse representation of EoSs predicting radii higher than DD2 will cause a significant underestimation of R for signals simulated using DD2. These non-uniformities in the EoS distribution introduce biases in the estimation of R . Addressing these biases will require either constructing a uniformly distributed EoS set or assigning a probability

to each EoS. We will explore these approaches in future studies.

V. RESULTS

Building on the Bayesian methodology outlined in Sec. IV, we performed model selection across ~ 2300 EoSs to compute their evidences for simulated BNS signals. These evidences were then used to derive radius posteriors, as detailed in this section.

A. Radius uncertainties from upgraded LVK and XG detectors

We present the uncertainties in R , with error bars indicating the 90% credible interval, for both companions from all BNS events with an SNR exceeding 10 in Fig. 4. These uncertainties are centered around the median value of $p(R|d_i)$. The SNR of each event is represented by a color bar (distinct for each detector network). A noticeable gap in the mass distribution around $2.1 M_\odot$ arises due to the double Gaussian population model, which provides little support in that region. To facilitate comparison, we overlay 5% bands around the EoS, indicating the

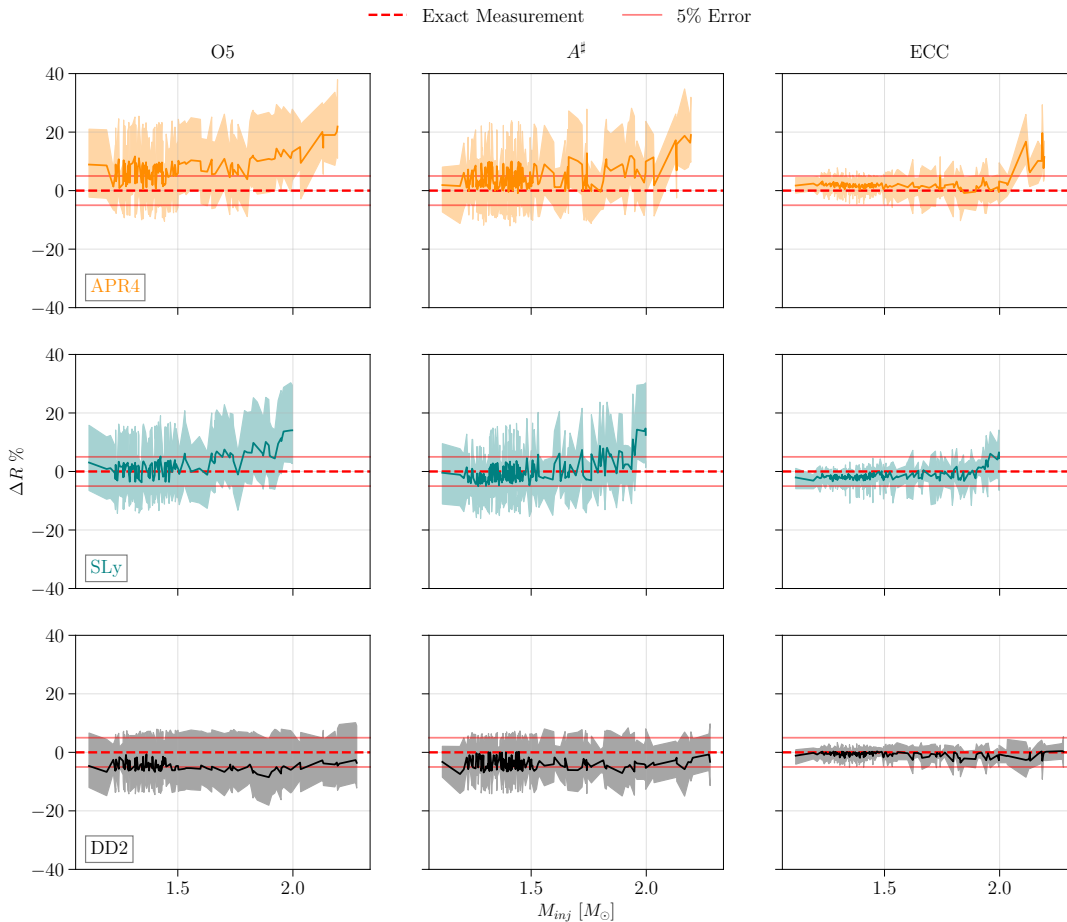


Figure 5. Fractional error percentage (ΔR) in the inferred value of R for the APR4, SLy, and DD2 (respectively top, middle, and bottom row) EoSs shown as a function of the injected NS masses. Different columns correspond to the considered detector sensitivities, increasing from left (O5) to right (ECC). The solid colored line for every EoS shows ΔR for the median value of the inferred posterior and the band around it shows the 90% credible interval. The red dashed line acts as a reference if there was no error and the red solid line shows 5% errors in ΔR . ΔR values corresponding to the O5 configuration are biased and the error is about 20%. The results are similar for A^\sharp with the R inference being inaccurate and imprecise. ECC shows a remarkable increase in accuracy and precisions as ΔR is constrained very well across all EoS to within 5% for almost the entire mass range.

radius variations expected for a uniform 5% change in the EoS.

Focusing on the O5 network, we observe significant uncertainties and systematic biases in most R estimates. Given a fixed detector sensitivity, these uncertainties primarily stem from the EoS dependence of R measurements. Softer EoSs, such as APR4 and SLy, predict smaller tidal deformability (Λ) values, resulting in a weaker tidal imprint on the gravitational wave (GW) signal and, consequently, broader uncertainties. This effect is particularly pronounced at higher masses, where tidal effects weaken as one approaches the binary black hole limit. Conversely, stiffer EoSs like DD2 predict larger Λ values, leading to stronger tidal effects and tighter constraints on R . This trend is reflected in our results, with uncertainties being most significant for APR4, intermediate for SLy, and smallest for DD2, although the differ-

ences may not always be visually distinct. For example, the uncertainty in R for the maximum-mass NS allowed by APR4 is approximately 16%, by SLy 14%, and by DD2 11%.

Beyond uncertainties, systematic biases also affect R estimates. For softer EoSs such as APR4 and SLy, the R posteriors tend to be systematically overestimated. This arises from constraints on Λ : since Λ must be positive, a hard boundary is imposed at $\Lambda = 0$. Weak constraints on Λ and minimal tidal effects in the GW waveform—especially in less sensitive networks like O5—amplify this bias, causing overestimated Λ values and, consequently, larger R values.

However, this explanation alone does not fully account for the results, as we also observe a systematic underestimation of R for stiffer EoSs like DD2. To better understand these biases, we refer to Fig. 2, which depicts

the distribution of EoS densities for a $1.4M_{\odot}$ NS across different radii. The density of EoSs peaks around the APR4 model, followed closely by SLy and DD2. A larger proportion of EoSs resembling APR4 predict radii larger than those predicted by APR4 itself, leading to an overestimation of R . Conversely, fewer EoSs resemble DD2 and those that do predict smaller radii, resulting in an underestimation of R for events analyzed with DD2.

These trends persist in the A^{\sharp} network, with only slight improvements in biases and uncertainties. This is primarily due to the relative sensitivity of the networks—O5 comprises four less sensitive networks, whereas A^{\sharp} consists of three more sensitive networks. Among these, the ECC network stands out, as most R measurements fall within the 5% EoS bands, and its radius estimates exhibit reduced biases compared to other networks.

Figure 5 summarizes our findings by illustrating the fractional percentage error ΔR as a function of injected mass across different EoSs and detector sensitivities. The key conclusion remains that for O5 and A^{\sharp} , the R estimates suffer from imprecision and inaccuracy. In contrast, ECC achieves superior accuracy, with ΔR remaining below 5% for most masses. For context, the average values of ΔR for SLy are 10%, 9%, and 4% for O5, A^{\sharp} , and ECC, respectively. The increase in ΔR at higher masses, previously noted, is also evident in this plot. However, ECC significantly mitigates this bias compared to other networks. While O5 and A^{\sharp} provide preliminary R estimates, ECC is required for reliable and precise constraints on R .

It is important to note that we do not specify a single numerical estimate for the lowest achievable radius uncertainty across networks, as uncertainties in R are inherently mass-dependent. Figure 5 demonstrates how uncertainties vary with mass, and quoting a single value would obscure this relationship. As the figure shows, for most EoSs, ECC maintains uncertainties below 5% across nearly the entire mass range. Thus, we recommend holistically interpreting Fig. 5, emphasizing the variation of uncertainties with mass rather than focusing on a specific value.

The accuracy of source mass estimates strongly depends on the precise inference of the luminosity distance and, consequently, the Hubble constant [84]. This dependence could introduce challenges in radius inference. However, since our analysis is limited to signals with redshift $z < 0.1$ and employs a consistent cosmological model for simulation and parameter estimation, these uncertainties do not significantly impact the inferred R posteriors.

B. Effect of mass priors

Figure 6 presents the cumulative radius uncertainties for the two mass priors considered: a double Gaussian prior, closely resembling the true NS mass distribution, and a uniform mass prior. Intuitively, one might expect

that a more realistic prior distribution would yield more precise radius measurements. However, as Fig. 6 illustrates, the uncertainties obtained using the two priors are nearly indistinguishable.

In the context of the ECC network, where SNRs are exceptionally high (typically ranging from 100 to 700, Fig. 4), parameter estimates are tightly constrained, and the likelihood dominates the prior. As a result, the influence of the prior is significantly diminished, leading to a close agreement between posteriors derived from different priors. Since both priors impose similar mass ranges, and the component masses are well-measured, this agreement also extends to O5 and A^{\sharp} . We provide further details on this in Appendix A.

VI. CONCLUSIONS

GW observations provide a powerful means to study NS properties, particularly their radii. However, due to the EoS dependence of these measurements, direct inference of NS radii from BNS signals remains challenging. In this work, we employ a model selection framework using multiple EoS models derived from GW170817 to construct a model-weighted radius posterior, mitigating reliance on any single EoS assumption. This approach offers insights into the ultra-dense matter within NSs without requiring direct EoS inference.

Fig. 5 demonstrates that the ECC network provides precise NS radius measurements, with uncertainties (ΔR) within 5% for stiffer EoSs like DD2. For softer EoSs such as APR4 and SLy, uncertainties remain within 5% in most cases. This underscores the capability of XG GW detector networks to refine NS property estimates. While the O5 and A^{\sharp} networks yield comparable uncertainties at times, their median radius values exhibit biases due to systematic overestimations of Λ and the density of EoS models used in selection. Addressing these biases and improving uncertainty estimates for O5 and A^{\sharp} remains a key objective for future studies. Furthermore, combining GW-inferred radii with multi-messenger observations can enhance EoS constraints.

Additionally, we investigate the role of astrophysically informed priors in Bayesian inference. Contrary to expectations, our results indicate that such priors do not significantly improve the accuracy of radius estimates compared to flat priors. This suggests that radius precision is predominantly dictated by the signal's loudness and the analysis methodology rather than prior assumptions about NS masses.

We therefore believe that our study advances our ability to infer NS properties from GW observations, offering valuable implications for nuclear physics and astrophysics. The projected precision in radius measurements will be instrumental in future observational and theoretical efforts to constrain the EoS and understand NS interiors.

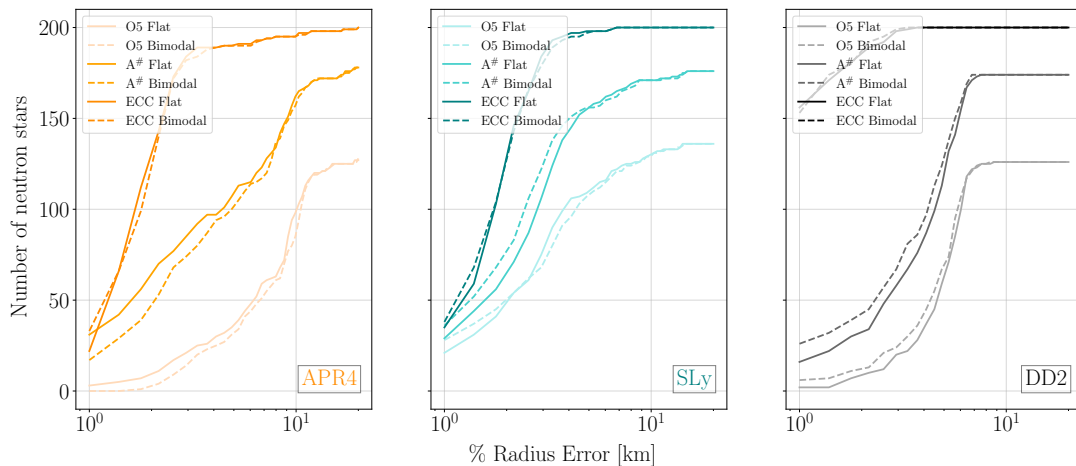


Figure 6. Comparing the radius uncertainties obtained with different priors on the NS mass for the APR4, SLy, and DD2 EoS. Solid lines show the uncertainty for a flat prior, while dotted orange lines represent those obtained using a double Gaussian prior. Within a single panel, the color gradient indicates the detector sensitivity variation from O5 being the lightest to ECC being the darkest. The obtained uncertainties don't change notably due to a change in the prior. It is also important to note that different networks detect different number of events, with ECC detecting the most and O5 detecting the least, which is also reflected in these panels.

VII. ACKNOWLEDGMENTS

We thank Geraint Pratten, Justin Janquart, and Bikram Pradhan for reviewing the BEOMS pipeline, which was critical for the Bayesian model selection used in this study. We also thank Lami Suleiman for reviewing the manuscript and Jacob Goulomb, Isaac Legred, Katerina Chatziioannou, and Reed Essick for their insightful comments. This research is supported by the National Science Foundation's (NSF) LIGO Labora-

tory. SK, IG, and BSS are also supported by NSF awards PHY-2207638, AST-2307147, PHY-2308886, and PHY-2309064, as well as by grants OAC-2346596, OAC-2201445, OAC-2103662, OAC-2018299, and PHY-2110594, which provided access to the GWAVE cluster at PennState. RG acknowledges support from NSF Grant PHY-2020275 (Network for Neutrinos, Nuclear Astrophysics, and Symmetries (N3AS)). This document is also available on LIGO DCC with the document number P2400544.

-
- [1] J. M. Lattimer, The nuclear equation of state and neutron star masses, *Ann. Rev. Nucl. Part. Sci.* **62**, 485 (2012), [arXiv:1305.3510 \[nucl-th\]](#).
 - [2] J. M. Lattimer and M. Prakash, The Equation of State of Hot, Dense Matter and Neutron Stars, *Phys. Rept.* **621**, 127 (2016), [arXiv:1512.07820 \[astro-ph.SR\]](#).
 - [3] F. Özel and P. Freire, Masses, Radii, and the Equation of State of Neutron Stars, *Ann. Rev. Astron. Astrophys.* **54**, 401 (2016), [arXiv:1603.02698 \[astro-ph.HE\]](#).
 - [4] A. L. Watts *et al.*, Colloquium : Measuring the neutron star equation of state using x-ray timing, *Rev. Mod. Phys.* **88**, 021001 (2016), [arXiv:1602.01081 \[astro-ph.HE\]](#).
 - [5] G. Baym, T. Hatsuda, T. Kojo, P. D. Powell, Y. Song, and T. Takatsuka, From hadrons to quarks in neutron stars: a review, *Rept. Prog. Phys.* **81**, 056902 (2018), [arXiv:1707.04966 \[astro-ph.HE\]](#).
 - [6] M. Oertel, M. Hempel, T. Klähn, and S. Typel, Equations of state for supernovae and compact stars, *Rev. Mod. Phys.* **89**, 015007 (2017), [arXiv:1610.03361 \[astro-ph.HE\]](#).
 - [7] V. Paschalidis and N. Stergioulas, Rotating Stars in Relativity, *Living Rev. Rel.* **20**, 7 (2017), [arXiv:1612.03050 \[astro-ph.HE\]](#).
 - [8] K. C. Gendreau, Z. Arzoumanian, P. W. Adkins, C. L. Albert, J. F. Anders, A. T. Aylward, C. L. Baker, E. R. Balsamo, W. A. Bamford, S. S. Benegalrao, D. L. Berry, S. Bhalwani, J. K. Black, C. Blaurock, G. M. Bronke, G. L. Brown, J. G. Budinoff, J. D. Cantwell, T. Cazeau, P. T. Chen, T. G. Clement, A. T. Colangelo, J. S. Coleman, J. D. Coopersmith, W. E. Dehaven, J. P. Doty, M. D. Egan, T. Enoto, T. W. Fan, D. M. Ferro, R. Foster, N. M. Galassi, L. D. Gallo, C. M. Green, D. Grosh, K. Q. Ha, M. A. Hasounch, K. B. Heefner, P. Hestnes, L. J. Hoge, T. M. Jacobs, J. L. Jørgensen, M. A. Kaiser, J. W. Kellogg, S. J. Kenyon, R. G. Koenecke, R. P. Kozon, B. LaMarr, M. D. Lambertson, A. M. Larson, S. Lentine, J. H. Lewis, M. G. Lilly, K. A. Liu, A. Malonis, S. S. Manthripragada, C. B. Markwardt, B. D. Matonak, I. E. Mcginnis, R. L. Miller, A. L. Mitchell, J. W. Mitchell, J. S. Mohammed, C. A. Monroe, K. M. Montt de Garcia, P. D. Mulé, L. T. Nagao, S. N. Ngo, E. D. Norris, D. A. Norwood, J. Novotka, T. Okajima,

- L. G. Olsen, C. O. Onyechu, H. Y. Orosco, J. R. Peterson, K. N. Pevear, K. K. Pham, S. E. Pollard, J. S. Pope, D. F. Powers, C. E. Powers, S. R. Price, G. Y. Prigozhin, J. B. Ramirez, W. J. Reid, R. A. Remillard, E. M. Rogstad, G. P. Rosecrans, J. N. Rowe, J. A. Sager, C. A. Sanders, B. Savadkin, M. R. Saylor, A. F. Schaeffer, N. S. Schweiss, S. R. Semper, P. J. Serlemittos, L. V. Shackelford, Y. Soong, J. Strubel, M. L. Vezie, J. S. Villasenor, L. B. Winternitz, G. I. Wofford, M. R. Wright, M. Y. Yang, and W. H. Yu, The Neutron star Interior Composition Explorer (NICER): design and development, in *Space Telescopes and Instrumentation 2016: Ultraviolet to Gamma Ray*, Society of Photo-Optical Instrumentation Engineers (SPIE) Conference Series, Vol. 9905, edited by J.-W. A. den Herder, T. Takahashi, and M. Bautz (2016) p. 99051H.
- [9] M. C. Miller *et al.*, PSR J0030+0451 Mass and Radius from *NICER* Data and Implications for the Properties of Neutron Star Matter, *Astrophys. J. Lett.* **887**, L24 (2019), [arXiv:1912.05705 \[astro-ph.HE\]](#).
- [10] M. C. Miller *et al.*, The Radius of PSR J0740+6620 from *NICER* and XMM-Newton Data, *Astrophys. J. Lett.* **918**, L28 (2021), [arXiv:2105.06979 \[astro-ph.HE\]](#).
- [11] G. Raaijmakers *et al.*, Constraining the dense matter equation of state with joint analysis of *NICER* and LIGO/Virgo measurements, *Astrophys. J. Lett.* **893**, L21 (2020), [arXiv:1912.11031 \[astro-ph.HE\]](#).
- [12] G. Raaijmakers *et al.*, A *NICER* view of PSR J0030+0451: Implications for the dense matter equation of state, *Astrophys. J. Lett.* **887**, L22 (2019), [arXiv:1912.05703 \[astro-ph.HE\]](#).
- [13] G. Raaijmakers, S. K. Greif, K. Hebeler, T. Hinderer, S. Nisanke, A. Schwenk, T. E. Riley, A. L. Watts, J. M. Lattimer, and W. C. G. Ho, Constraints on the Dense Matter Equation of State and Neutron Star Properties from *NICER*'s Mass-Radius Estimate of PSR J0740+6620 and Multimessenger Observations, *Astrophys. J. Lett.* **918**, L29 (2021), [arXiv:2105.06981 \[astro-ph.HE\]](#).
- [14] S. Bogdanov *et al.*, Constraining the Neutron Star Mass-Radius Relation and Dense Matter Equation of State with *NICER*. I. The Millisecond Pulsar X-Ray Data Set, *Astrophys. J. Lett.* **887**, L25 (2019), [arXiv:1912.05706 \[astro-ph.HE\]](#).
- [15] S. Bogdanov *et al.*, Constraining the Neutron Star Mass-Radius Relation and Dense Matter Equation of State with *NICER*. II. Emission from Hot Spots on a Rapidly Rotating Neutron Star, *Astrophys. J. Lett.* **887**, L26 (2019), [arXiv:1912.05707 \[astro-ph.HE\]](#).
- [16] X. Roca-Maza, M. Centelles, X. Vinas, and M. Warda, Neutron skin of ^{208}Pb , nuclear symmetry energy, and the parity radius experiment, *Phys. Rev. Lett.* **106**, 252501 (2011), [arXiv:1103.1762 \[nucl-th\]](#).
- [17] F. J. Fattoyev, J. Piekarewicz, and C. J. Horowitz, Neutron Skins and Neutron Stars in the Multimessenger Era, *Phys. Rev. Lett.* **120**, 172702 (2018), [arXiv:1711.06615 \[nucl-th\]](#).
- [18] B. T. Reed, F. J. Fattoyev, C. J. Horowitz, and J. Piekarewicz, Implications of PREX-2 on the Equation of State of Neutron-Rich Matter, *Phys. Rev. Lett.* **126**, 172503 (2021), [arXiv:2101.03193 \[nucl-th\]](#).
- [19] B. P. Abbott *et al.* (LIGO Scientific, Virgo), GW170817: Observation of Gravitational Waves from a Binary Neutron Star Inspiral, *Phys. Rev. Lett.* **119**, 161101 (2017), [arXiv:1710.05832 \[gr-qc\]](#).
- [20] B. P. Abbott *et al.* (LIGO Scientific, Virgo), GW190425: Observation of a Compact Binary Coalescence with Total Mass $\sim 3.4M_{\odot}$, *Astrophys. J. Lett.* **892**, L3 (2020), [arXiv:2001.01761 \[astro-ph.HE\]](#).
- [21] J. Aasi *et al.* (LIGO Scientific), Advanced LIGO, *Class. Quant. Grav.* **32**, 074001 (2015), [arXiv:1411.4547 \[gr-qc\]](#).
- [22] F. Acernese *et al.* (VIRGO), Advanced Virgo: a second-generation interferometric gravitational wave detector, *Class. Quant. Grav.* **32**, 024001 (2015), [arXiv:1408.3978 \[gr-qc\]](#).
- [23] B. P. Abbott *et al.* (LIGO Scientific, Virgo, Fermi-GBM, INTEGRAL), Gravitational Waves and Gamma-rays from a Binary Neutron Star Merger: GW170817 and GRB 170817A, *Astrophys. J. Lett.* **848**, L13 (2017), [arXiv:1710.05834 \[astro-ph.HE\]](#).
- [24] D. Radice, A. Perego, F. Zappa, and S. Bernuzzi, GW170817: Joint Constraint on the Neutron Star Equation of State from Multimessenger Observations, *Astrophys. J. Lett.* **852**, L29 (2018), [arXiv:1711.03647 \[astro-ph.HE\]](#).
- [25] M. W. Coughlin, T. Dietrich, B. Margalit, and B. D. Metzger, Multimessenger Bayesian parameter inference of a binary neutron star merger, *Mon. Not. Roy. Astron. Soc.* **489**, L91 (2019), [arXiv:1812.04803 \[astro-ph.HE\]](#).
- [26] C. A. Raithel, Constraints on the Neutron Star Equation of State from GW170817, *Eur. Phys. J. A* **55**, 80 (2019), [arXiv:1904.10002 \[astro-ph.HE\]](#).
- [27] C. D. Capano, I. Tews, S. M. Brown, B. Margalit, S. De, S. Kumar, D. A. Brown, B. Krishnan, and S. Reddy, Stringent constraints on neutron-star radii from multimessenger observations and nuclear theory, *Nature Astron.* **4**, 625 (2020), [arXiv:1908.10352 \[astro-ph.HE\]](#).
- [28] M. Breschi, R. Gamba, G. Carullo, D. Godzieba, S. Bernuzzi, A. Perego, and D. Radice, Bayesian inference of multimessenger astrophysical data: Joint and coherent inference of gravitational waves and kilonovae, *Astron. Astrophys.* **689**, A51 (2024), [arXiv:2401.03750 \[astro-ph.HE\]](#).
- [29] H. Koehn *et al.*, From existing and new nuclear and astrophysical constraints to stringent limits on the equation of state of neutron-rich dense matter (2024), [arXiv:2402.04172 \[astro-ph.HE\]](#).
- [30] A. Ayriyan, D. Blaschke, A. G. Grunfeld, D. Alvarez-Castillo, H. Grigorian, and V. Abgaryan, Bayesian analysis of multimessenger M-R data with interpolated hybrid EoS, *Eur. Phys. J. A* **57**, 318 (2021), [arXiv:2102.13485 \[astro-ph.HE\]](#).
- [31] R. Essick, I. Tews, P. Landry, S. Reddy, and D. E. Holz, Direct Astrophysical Tests of Chiral Effective Field Theory at Supranuclear Densities, *Phys. Rev. C* **102**, 055803 (2020), [arXiv:2004.07744 \[astro-ph.HE\]](#).
- [32] J. Hu, S. Bao, Y. Zhang, K. Nakazato, K. Sumiyoshi, and H. Shen, Effects of symmetry energy on the radius and tidal deformability of neutron stars in the relativistic mean-field model, *PTEP* **2020**, 043D01 (2020), [arXiv:2002.00562 \[nucl-th\]](#).
- [33] T. Akutsu *et al.* (KAGRA), Overview of KAGRA: Detector design and construction history, *PTEP* **2021**, 05A101 (2021), [arXiv:2005.05574 \[physics.ins-det\]](#).
- [34] L. Barsotti, L. McCuller, M. Evans, and P. Fritschel, *The A+ Design Curve*, Tech. Rep. T1800042 (LIGO, 2018).

- [35] P. Fritschel, K. Kuns, J. Driggers, A. Effler, B. Lantz, D. Ottaway, S. Ballmer, K. Dooley, R. Adhikari, M. Evans, B. Farr, G. Gonzalez, P. Schmidt, and S. Raja, *Report from the LSC Post-O5 Study Group*, Tech. Rep. T2200287 (LIGO, 2022).
- [36] D. Reitze *et al.*, Cosmic Explorer: The U.S. Contribution to Gravitational-Wave Astronomy beyond LIGO, *Bull. Am. Astron. Soc.* **51**, 035 (2019), [arXiv:1907.04833 \[astro-ph.IM\]](#).
- [37] M. Evans *et al.*, A Horizon Study for Cosmic Explorer: Science, Observatories, and Community (2021), [arXiv:2109.09882 \[astro-ph.IM\]](#).
- [38] B. P. Abbott *et al.* (LIGO Scientific), Exploring the Sensitivity of Next Generation Gravitational Wave Detectors, *Class. Quant. Grav.* **34**, 044001 (2017), [arXiv:1607.08697 \[astro-ph.IM\]](#).
- [39] M. Punturo *et al.*, The third generation of gravitational wave observatories and their science reach, *Class. Quant. Grav.* **27**, 084007 (2010).
- [40] S. Hild *et al.*, Sensitivity Studies for Third-Generation Gravitational Wave Observatories, *Class. Quant. Grav.* **28**, 094013 (2011), [arXiv:1012.0908 \[gr-qc\]](#).
- [41] M. Maggiore *et al.* (ET), Science Case for the Einstein Telescope, *JCAP* **03** (3), 050, [arXiv:1912.02622 \[astro-ph.CO\]](#).
- [42] I. Gupta *et al.*, Characterizing gravitational wave detector networks: from A[#] to cosmic explorer, *Class. Quant. Grav.* **41**, 245001 (2024), [arXiv:2307.10421 \[gr-qc\]](#).
- [43] L. K. Tsui and P.-T. Leung, Probing the interior of neutron stars with gravitational waves, *Phys. Rev. Lett.* **95**, 151101 (2005), [arXiv:astro-ph/0506681](#).
- [44] M. Agathos, J. Meidam, W. Del Pozzo, T. G. F. Li, M. Tompitak, J. Veitch, S. Vitale, and C. Van Den Broeck, Constraining the neutron star equation of state with gravitational wave signals from coalescing binary neutron stars, *Phys. Rev. D* **92**, 023012 (2015), [arXiv:1503.05405 \[gr-qc\]](#).
- [45] B. D. Lackey and L. Wade, Reconstructing the neutron-star equation of state with gravitational-wave detectors from a realistic population of inspiralling binary neutron stars, *Phys. Rev. D* **91**, 043002 (2015), [arXiv:1410.8866 \[gr-qc\]](#).
- [46] F. Hernandez Vivanco, R. Smith, E. Thrane, P. D. Lasky, C. Talbot, and V. Raymond, Measuring the neutron star equation of state with gravitational waves: The first forty binary neutron star merger observations, *Phys. Rev. D* **100**, 103009 (2019), [arXiv:1909.02698 \[gr-qc\]](#).
- [47] P. Landry and R. Essick, Nonparametric inference of the neutron star equation of state from gravitational wave observations, *Phys. Rev. D* **99**, 084049 (2019), [arXiv:1811.12529 \[gr-qc\]](#).
- [48] K. Chatziioannou and W. M. Farr, Inferring the maximum and minimum mass of merging neutron stars with gravitational waves, *Phys. Rev. D* **102**, 064063 (2020), [arXiv:2005.00482 \[astro-ph.HE\]](#).
- [49] Wysocki, Daniel and O’Shaughnessy, Richard and Wade, Leslie and Lange, Jacob, Inferring the neutron star equation of state simultaneously with the population of merging neutron stars (2020), [arXiv:2001.01747 \[gr-qc\]](#).
- [50] J. Golomb and C. Talbot, Hierarchical Inference of Binary Neutron Star Mass Distribution and Equation of State with Gravitational Waves, *Astrophys. J.* **926**, 79 (2022), [arXiv:2106.15745 \[astro-ph.HE\]](#).
- [51] P. Landry, R. Essick, and K. Chatziioannou, Nonparametric constraints on neutron star matter with existing and upcoming gravitational wave and pulsar observations, *Phys. Rev. D* **101**, 123007 (2020), [arXiv:2003.04880 \[astro-ph.HE\]](#).
- [52] R. Essick, P. Landry, and D. E. Holz, Nonparametric Inference of Neutron Star Composition, Equation of State, and Maximum Mass with GW170817, *Phys. Rev. D* **101**, 063007 (2020), [arXiv:1910.09740 \[astro-ph.HE\]](#).
- [53] A. Ray, I. Magaña Hernandez, S. Mohite, J. Creighton, and S. Kapadia, Nonparametric Inference of the Population of Compact Binaries from Gravitational-wave Observations Using Binned Gaussian Processes, *Astrophys. J.* **957**, 37 (2023), [arXiv:2304.08046 \[gr-qc\]](#).
- [54] T. Ghosh, B. Biswas, and S. Bose, Simultaneous inference of neutron star equation of state and the Hubble constant with a population of merging neutron stars, *Phys. Rev. D* **106**, 123529 (2022), [arXiv:2203.11756 \[astro-ph.CO\]](#).
- [55] B. K. Pradhan, D. Pathak, and D. Chatterjee, Constraining Nuclear Parameters Using Gravitational Waves from f-mode Oscillations in Neutron Stars, *Astrophys. J.* **956**, 38 (2023), [arXiv:2306.04626 \[astro-ph.HE\]](#).
- [56] B. K. Pradhan, T. Ghosh, D. Pathak, and D. Chatterjee, Cost of Inferred Nuclear Parameters toward the f-mode Dynamical Tide in Binary Neutron Stars, *Astrophys. J.* **966**, 79 (2024), [arXiv:2311.16561 \[gr-qc\]](#).
- [57] D. Finstad, L. V. White, and D. A. Brown, Prospects for a Precise Equation of State Measurement from Advanced LIGO and Cosmic Explorer, *Astrophys. J.* **955**, 45 (2023), [arXiv:2211.01396 \[astro-ph.HE\]](#).
- [58] A. Bandopadhyay, K. Kacanja, R. Somasundaram, A. H. Nitz, and D. A. Brown, Measuring neutron star radius with second and third generation gravitational wave detector networks, *Class. Quant. Grav.* **41**, 225003 (2024), [arXiv:2402.05056 \[astro-ph.HE\]](#).
- [59] S. De, D. Finstad, J. M. Lattimer, D. A. Brown, E. Berger, and C. M. Biwer, Tidal Deformabilities and Radii of Neutron Stars from the Observation of GW170817, *Phys. Rev. Lett.* **121**, 091102 (2018), [Erratum: *Phys.Rev.Lett.* 121, 259902 (2018)], [arXiv:1804.08583 \[astro-ph.HE\]](#).
- [60] R. Huxford, R. Kashyap, S. Borhanian, A. Dhani, I. Gupta, and B. S. Sathyaprakash, Accuracy of neutron star radius measurement with the next generation of terrestrial gravitational-wave observatories, *Phys. Rev. D* **109**, 103035 (2024), [arXiv:2307.05376 \[gr-qc\]](#).
- [61] K. Walker, R. Smith, E. Thrane, and D. J. Reardon, Precision constraints on the neutron star equation of state with third-generation gravitational-wave observatories, *Phys. Rev. D* **110**, 043013 (2024), [arXiv:2401.02604 \[astro-ph.HE\]](#).
- [62] L. Lindblom, Spectral Representations of Neutron-Star Equations of State, *Phys. Rev. D* **82**, 103011 (2010), [arXiv:1009.0738 \[astro-ph.HE\]](#).
- [63] B. P. Abbott *et al.* (LIGO Scientific, Virgo), GW170817: Measurements of neutron star radii and equation of state, *Phys. Rev. Lett.* **121**, 161101 (2018), [arXiv:1805.11581 \[gr-qc\]](#).
- [64] LIGO Scientific Collaboration, Parametrized Equation of State: Maximum mass posterior samples, <https://dcc.ligo.org/public/0152/P1800115/005/>

- [Parametrized-EoS_maxmass_posterior_samples.dat](#) (2018).
- [65] T. Futamase and Y. Itoh, The post-Newtonian approximation for relativistic compact binaries, *Living Rev. Rel.* **10**, 2 (2007).
- [66] L. Blanchet, Post-Newtonian Theory for Gravitational Waves, *Living Rev. Rel.* **17**, 2 (2014), [arXiv:1310.1528 \[gr-qc\]](#).
- [67] R. A. Porto, The effective field theorist’s approach to gravitational dynamics, *Phys. Rept.* **633**, 1 (2016), [arXiv:1601.04914 \[hep-th\]](#).
- [68] M. Levi, Effective Field Theories of Post-Newtonian Gravity: A comprehensive review, *Rept. Prog. Phys.* **83**, 075901 (2020), [arXiv:1807.01699 \[hep-th\]](#).
- [69] T. Hinderer, Tidal Love numbers of neutron stars, *Astrophys. J.* **677**, 1216 (2008), [Erratum: *Astrophys. J.* **697**, 964 (2009)], [arXiv:0711.2420 \[astro-ph\]](#).
- [70] E. E. Flanagan and T. Hinderer, Constraining neutron star tidal Love numbers with gravitational wave detectors, *Phys. Rev. D* **77**, 021502 (2008), [arXiv:0709.1915 \[astro-ph\]](#).
- [71] J. Vines, E. E. Flanagan, and T. Hinderer, Post-1-Newtonian tidal effects in the gravitational waveform from binary inspirals, *Phys. Rev. D* **83**, 084051 (2011), [arXiv:1101.1673 \[gr-qc\]](#).
- [72] L. Wade, J. D. E. Creighton, E. Ochsner, B. D. Lackey, B. F. Farr, T. B. Littenberg, and V. Raymond, Systematic and statistical errors in a bayesian approach to the estimation of the neutron-star equation of state using advanced gravitational wave detectors, *Phys. Rev. D* **89**, 103012 (2014), [arXiv:1402.5156 \[gr-qc\]](#).
- [73] A. Buonanno and T. Damour, Effective one-body approach to general relativistic two-body dynamics, *Phys. Rev. D* **59**, 084006 (1999), [arXiv:gr-qc/9811091](#).
- [74] A. Buonanno and T. Damour, Transition from inspiral to plunge in binary black hole coalescences, *Phys. Rev. D* **62**, 064015 (2000), [arXiv:gr-qc/0001013](#).
- [75] T. Damour, Coalescence of two spinning black holes: an effective one-body approach, *Phys. Rev. D* **64**, 124013 (2001), [arXiv:gr-qc/0103018](#).
- [76] P. Ajith *et al.*, Inspiral-merger-ringdown waveforms for black-hole binaries with non-precessing spins, *Phys. Rev. Lett.* **106**, 241101 (2011), [arXiv:0909.2867 \[gr-qc\]](#).
- [77] L. Santamaria *et al.*, Matching post-Newtonian and numerical relativity waveforms: systematic errors and a new phenomenological model for non-precessing black hole binaries, *Phys. Rev. D* **82**, 064016 (2010), [arXiv:1005.3306 \[gr-qc\]](#).
- [78] G. Pratten, S. Husa, C. Garcia-Quiros, M. Colleoni, A. Ramos-Buades, H. Estelles, and R. Jaume, Setting the cornerstone for a family of models for gravitational waves from compact binaries: The dominant harmonic for nonprecessing quasicircular black holes, *Phys. Rev. D* **102**, 064001 (2020), [arXiv:2001.11412 \[gr-qc\]](#).
- [79] T. Dietrich *et al.*, Matter imprints in waveform models for neutron star binaries: Tidal and self-spin effects, *Phys. Rev. D* **99**, 024029 (2019), [arXiv:1804.02235 \[gr-qc\]](#).
- [80] T. Dietrich, A. Samajdar, S. Khan, N. K. Johnson-McDaniel, R. Dudi, and W. Tichy, Improving the NR-Tidal model for binary neutron star systems, *Phys. Rev. D* **100**, 044003 (2019), [arXiv:1905.06011 \[gr-qc\]](#).
- [81] S. Khan, S. Husa, M. Hannam, F. Ohme, M. Pürrer, X. Jiménez Forteza, and A. Bohé, Frequency-domain gravitational waves from nonprecessing black-hole binaries. II. A phenomenological model for the advanced detector era, *Phys. Rev. D* **93**, 044007 (2016), [arXiv:1508.07253 \[gr-qc\]](#).
- [82] S. Husa, S. Khan, M. Hannam, M. Pürrer, F. Ohme, X. Jiménez Forteza, and A. Bohé, Frequency-domain gravitational waves from nonprecessing black-hole binaries. I. New numerical waveforms and anatomy of the signal, *Phys. Rev. D* **93**, 044006 (2016), [arXiv:1508.07250 \[gr-qc\]](#).
- [83] European Gravitational Observatory, [Et-0304b-22: Etsensitivitycurvesusedforcoba](#) (2022), accessed: 2024-12-19.
- [84] I. M. Romero-Shaw *et al.*, Bayesian inference for compact binary coalescences with bilby: validation and application to the first LIGO–Virgo gravitational-wave transient catalogue, *Mon. Not. Roy. Astron. Soc.* **499**, 3295 (2020), [arXiv:2006.00714 \[astro-ph.IM\]](#).
- [85] G. Ashton *et al.*, BILBY: A user-friendly Bayesian inference library for gravitational-wave astronomy, *Astrophys. J. Suppl.* **241**, 27 (2019), [arXiv:1811.02042 \[astro-ph.IM\]](#).
- [86] LIGO Scientific Collaboration, Virgo Collaboration, and KAGRA Collaboration, [LVK Algorithm Library - LALSuite](#), Free software (GPL) (2018).
- [87] K. Wette, SWIGLAL: Python and Octave interfaces to the LALSuite gravitational-wave data analysis libraries, *SoftwareX* **12**, 100634 (2020).
- [88] J. S. Speagle, dynesty: a dynamic nested sampling package for estimating Bayesian posteriors and evidences, *Mon. Not. Roy. Astron. Soc.* **493**, 3132 (2020), [arXiv:1904.02180 \[astro-ph.IM\]](#).
- [89] N. J. Cornish, Fast Fisher Matrices and Lazy Likelihoods (2010), [arXiv:1007.4820 \[gr-qc\]](#).
- [90] N. J. Cornish, Heterodyned likelihood for rapid gravitational wave parameter inference, *Phys. Rev. D* **104**, 104054 (2021), [arXiv:2109.02728 \[gr-qc\]](#).
- [91] B. Zackay, L. Dai, and T. Venumadhav, Relative Binning and Fast Likelihood Evaluation for Gravitational Wave Parameter Estimation (2018), [arXiv:1806.08792 \[astro-ph.IM\]](#).
- [92] K. Krishna, A. Vijaykumar, A. Ganguly, C. Talbot, S. Biscoveanu, R. N. George, N. Williams, and A. Zimmerman, Accelerated parameter estimation in Bilby with relative binning (2023), [arXiv:2312.06009 \[gr-qc\]](#).
- [93] B. P. Abbott *et al.* (KAGRA, LIGO Scientific, Virgo, VIRGO), Prospects for observing and localizing gravitational-wave transients with Advanced LIGO, Advanced Virgo and KAGRA, *Living Rev. Rel.* **21**, 3 (2018), [arXiv:1304.0670 \[gr-qc\]](#).
- [94] C. S. Unnikrishnan, IndIGO and LIGO-India: Scope and plans for gravitational wave research and precision metrology in India, *Int. J. Mod. Phys. D* **22**, 1341010 (2013), [arXiv:1510.06059 \[physics.ins-det\]](#).
- [95] M. Saleem *et al.*, The science case for LIGO-India, *Class. Quant. Grav.* **39**, 025004 (2022), [arXiv:2105.01716 \[gr-qc\]](#).
- [96] S. Pandey, I. Gupta, K. Chandra, and B. S. Sathyaprakash, The Critical Role of LIGO-India in the Era of Next-Generation Observatories (2024), [arXiv:2411.10349 \[gr-qc\]](#).
- [97] R. Abbott *et al.* (LIGO Scientific, Virgo), Population Properties of Compact Objects from the Second LIGO–Virgo Gravitational-Wave Transient Catalog, *Astro-*

- phys. J. Lett. **913**, L7 (2021), arXiv:2010.14533 [astro-ph.HE].
- [98] J. Antoniadis, T. M. Tauris, F. Özel, E. Barr, D. J. Champion, and P. C. C. Freire, The millisecond pulsar mass distribution: Evidence for bimodality and constraints on the maximum neutron star mass (2016), arXiv:1605.01665 [astro-ph.HE].
- [99] J. Alsing, H. O. Silva, and E. Berti, Evidence for a maximum mass cut-off in the neutron star mass distribution and constraints on the equation of state, *Mon. Not. Roy. Astron. Soc.* **478**, 1377 (2018), arXiv:1709.07889 [astro-ph.HE].
- [100] W. M. Farr and K. Chatziioannou, A Population-Informed Mass Estimate for Pulsar J0740+6620, *Research Notes of the American Astronomical Society* **4**, 65 (2020), arXiv:2005.00032 [astro-ph.GA].
- [101] D.-S. Shao, S.-P. Tang, J.-L. Jiang, and Y.-Z. Fan, Maximum mass cutoff in the neutron star mass distribution and the prospect of forming supramassive objects in the double neutron star mergers, *Phys. Rev. D* **102**, 063006 (2020), arXiv:2009.04275 [astro-ph.HE].
- [102] P. Landry and J. S. Read, The Mass Distribution of Neutron Stars in Gravitational-wave Binaries, *Astrophys. J. Lett.* **921**, L25 (2021), arXiv:2107.04559 [astro-ph.HE].
- [103] B. P. Abbott *et al.* (LIGO Scientific, Virgo), Model comparison from LIGO–Virgo data on GW170817’s binary components and consequences for the merger remnant, *Class. Quant. Grav.* **37**, 045006 (2020), arXiv:1908.01012 [gr-qc].
- [104] S. Nissanke, D. E. Holz, S. A. Hughes, N. Dalal, and J. L. Sievers, Exploring short gamma-ray bursts as gravitational-wave standard sirens, *Astrophys. J.* **725**, 496 (2010), arXiv:0904.1017 [astro-ph.CO].
- [105] B. Ewing *et al.*, Performance of the low-latency GstLAL inspiral search towards LIGO, Virgo, and KAGRA’s fourth observing run, *Phys. Rev. D* **109**, 042008 (2024), arXiv:2305.05625 [gr-qc].
- [106] J. Veitch *et al.*, Parameter estimation for compact binaries with ground-based gravitational-wave observations using the LALInference software library, *Phys. Rev. D* **91**, 042003 (2015), arXiv:1409.7215 [gr-qc].
- [107] R. Abbott *et al.* (LIGO Scientific, Virgo), GWTC-2: Compact Binary Coalescences Observed by LIGO and Virgo During the First Half of the Third Observing Run, *Phys. Rev. X* **11**, 021053 (2021), arXiv:2010.14527 [gr-qc].
- [108] R. Kashyap, I. Gupta, A. Dhani, M. Bapna, and B. Sathyaprakash, Optimizing Bayesian model selection for equation of state of cold neutron stars, in prep (2024).

Appendix A: Details about Mass Priors

In Fig. 6, we compare the radius uncertainties obtained using the bimodal prior and the uniform priors.

We conclude that on an individual event level, the uncertainties do not differ much for different detector sensitivities and EoSs. In this appendix, we present a few more nuances about the reasoning behind such trends.

To gain insight into the prior distributions, we analyze two events using the O5 sensitivity and the SLy EoS. These events are chosen so that the heavier component mass, m_1 , corresponds to the two peaks of the bimodal distribution, where the uniform and bimodal priors are expected to differ the most. Figure 7 compares the prior samples drawn from the bimodal and uniform distributions for m_1 and shows the error in the measurement of m_1 for both events. For the event at the secondary peak, with $m_1 = 1.8M_\odot$, the priors align in the range relevant for posterior inference. Even for the event at the primary peak, with $m_1 = 1.34M_\odot$, where the prior distributions are expected to differ the most, the variation remains small to impact the mass posteriors. The posteriors are well constrained, as indicated by the gray band. To affect the results, the priors would need to be significantly different in a narrow mass range, which is not the case in Fig. 7. As a direct consequence, Fig. 8 shows that the median values of the inferred mass posteriors remain consistent across both priors. Therefore, the radius uncertainties inferred using these priors do not show significant differences.

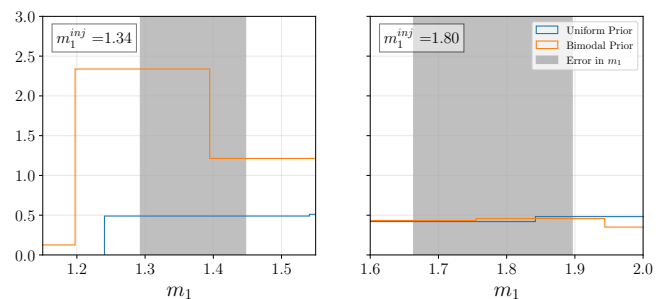


Figure 7. *Left panel*: Prior samples drawn from the bimodal and uniform prior distributions for the heavier component mass m_1 for an example event having $m_1 = 1.34$. The gray band represents the uncertainty in the inferred value of m_1 for this event. *Right panel*: A similar plot with another example event having higher $m_1 = 1.80$. The prior do not differ significantly from each other in the 1σ range of the inferred posterior leading to little to no effects on the inferred radius uncertainty values.

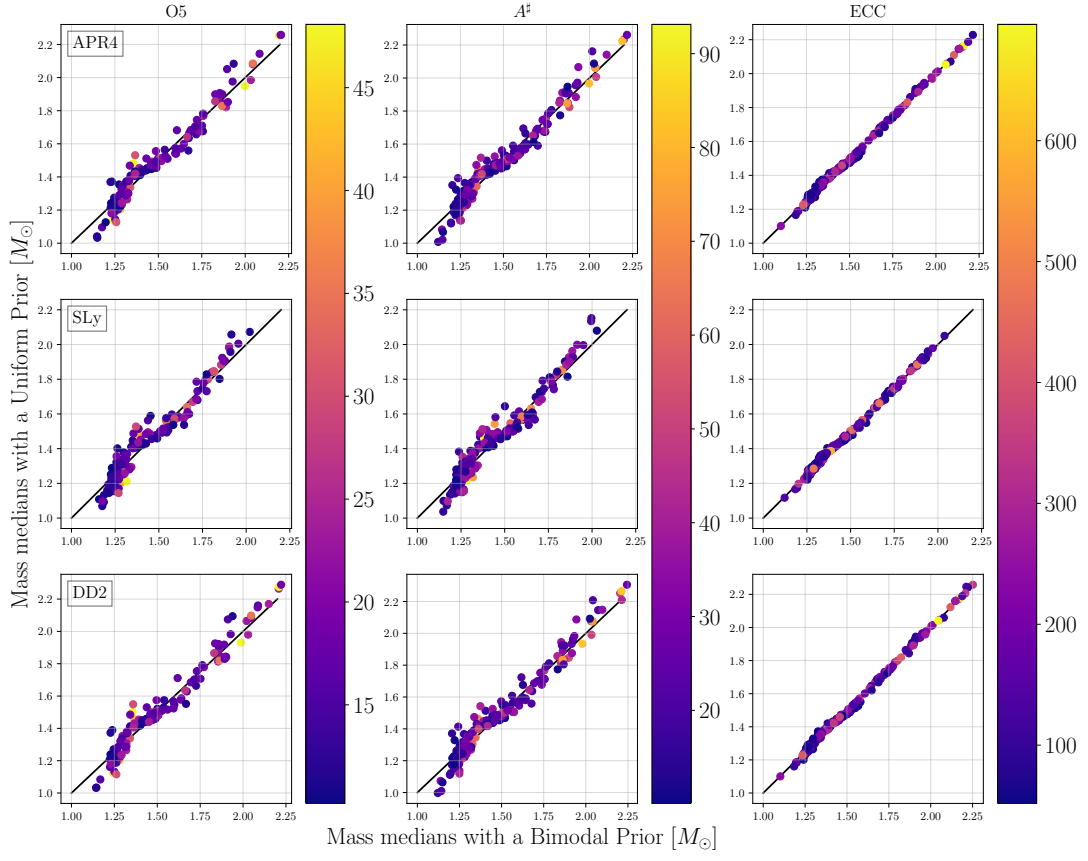


Figure 8. Comparison of the median values of the posterior distributions for the heavier component mass, m_1 , obtained using the uniform and bimodal priors. Since the prior distributions do not vary significantly over narrow mass ranges, the median values from both distributions remain largely consistent. The color bar represents the SNR of the events, providing context for those that deviate from the equality line.